The dielectric function profile across the water interface through surface-specific vibrational spectroscopy and simulations

Kuo-Yang Chiang[a], Takakazu Seki[a], Chun-Chieh Yu[a], Tatsuhiko Ohto[b], Johannes Hunger[a], Mischa Bonn[a], and Yuki Nagata[a,1]

The dielectric properties of interfacial water on subnanometer length scales govern chemical reactions, carrier transfer, and ion transport at interfaces. Yet, the nature of the interfacial dielectric function has remained under debate as it is challenging to access the interfacial dielectric with subnanometer resolution. Here we use the vibrational response of interfacial water molecules probed using surface-specific sum-frequency generation (SFG) spectra to obtain exquisite depth resolution. Different responses originate from water molecules at different depths and report back on the local interfacial dielectric environment via their spectral amplitudes. From experimental and simulated SFG spectra at the air/water interface, we find that the interfacial dielectric constant changes drastically across an ~1 Å thin interfacial water region. The strong gradient of the interfacial dielectric constant leads, at charged planar interfaces, to the formation of an electric triple layer that goes beyond the standard double-layer model.

interfacial water | dielectric function | vibrational spectroscopy | molecular dynamics simulation

The dielectric properties of aqueous interfaces within thicknesses of <1 nm control chemical reaction processes and proton transfer at interfaces, affecting many natural phenomena ranging from on-water atmospheric chemical reactions to electrical device performance (1–3). For example, the interfacial dielectric constant of water governs the surface potential and determines the double-layer capacitance (4). The measured proton transport across the single-layer material shows a lower activation barrier (5) than expected (6, 7), implying that electric double-layer models based on a homogeneous dielectric continuum provide a poor description of the interface (8). Although simulations have predicted that the dielectric profile of water varies drastically across the interfacial region (4), experimentally, it is challenging to obtain molecular-level insight into the interfacial dielectric function. For example, the experimental observables in capacitance measurements are ensemble averages over the entire system (9, 10), prohibitive of disentangling the depth variation of the interfacial dielectric properties. The dielectric constant of systems with water confined in nanometer-sized channels has been measured (9), yet the contribution of water to the system's response is under debate (11), and information on subnanometer length scales is lacking.

Experimental verification on the subnanometer depth variation of the interfacial dielectric requires layer-by-layer resolution of interfacial water. Sum-frequency generation (SFG) spectroscopy (12–14) is excellently suited to spatially resolve interfacial water. In SFG, infrared (IR) and visible pulses generate an SFG signal at their sum-frequency in a surface-specific second-order nonlinear process. Furthermore, the SFG signal is enhanced when the IR pulse frequency is resonant with a molecular vibration, allowing us to specifically detect molecular moieties. Such a frequency-dependent SFG signal can be linked to interfacial water molecules at different depths. For example, the spectrum of water's O–H stretch mode at the air/water interface shows a positive $3,700~\text{cm}^{-1}$ and a negative $3,400~\text{cm}^{-1}$ feature (15). The $3,700~\text{cm}^{-1}$ peak arises from the dangling O–H stretch mode of the topmost water molecules, while the $3,400~\text{cm}^{-1}$ peak arises from the hydrogen-bonded (H-bonded) O–H stretch mode of the first one to two layers of interfacial water molecules (16–18). The experimental SFG spectra necessarily reflect the interfacial dielectric environment (19), since the local dielectric function determines the strength of the local electromagnetic field used in the measurement. As such, the SFG spectra of the free O–H and H-bonded O–H stretch modes of water at the air/water interface can provide information on the variation of the interfacial dielectric properties in the topmost one to two layers.

To infer the interfacial dielectric profile, one needs to compare the experimentally measured SFG spectra with the simulated molecular response (13). Accurate experimental SFG spectra are now accessible thanks to the recent advances in precise phase determination in heterodyne-detected SFG experiments (15). The ab initio force field

Significance

The dielectric properties of interfacial water on subnanometer length scales govern chemical reactions, electron transfer, and ion transport at interfaces. For example, the double-layer capacitance is strongly affected by the interfacial dielectric constant. The stabilization of molecules at interfaces is also governed by the dielectric constant of water in the Onsager–Samalas model, where ions are repelled from the air/water interface by their image charges on the air side. Despite its environmental importance and technological relevance, we have minimal understanding of the dielectric properties of interfacial water at the angstrom level due to the lack of experimental techniques accessible to the interfaces. Here we resolve the interfacial dielectric function with the angstrom-level depth resolution through surface-specific vibrational spectroscopy and simulation.

models of water, such as the polarizable water model for intramolecular and intermolecular vibrational spectroscopies (POLI2VS) and many-body potential for water (MB-pol) models, can accurately reproduce experimental line shapes as well as the absolute amplitudes of the vibrational spectra of bulk water (20, 21) and have been successfully applied to simulate the SFG spectra of water (22, 23). Combining these experimental and simulation techniques allows us to access the interfacial dielectric profile.

The interfacial dielectric function (ε') is required to relate the experimentally measured line shapes (13) and absolute amplitudes (24) of water's O–H stretch mode to the simulated molecular response. Here the xz plane forms the incident plane of the laser beams, and the z axis is the surface normal. The ε'-uncorrected SFG spectrum in zzz polarization direction ($\chi'^{(2)}_{zzz}$) is experimentally accessible from the SFG signals at the ssp and ppp polarizations [denoted as $(\chi^{(2)}_{\exp})_{ssp}$ and $(\chi^{(2)}_{\exp})_{ppp}$, respectively] via

$$\chi'^{(2)}_{zzz} = \frac{\sqrt{2}\left(2(\chi^{(2)}_{\exp})_{ppp} + \frac{L_{xx}(\omega)L_{xx}(\omega_1)}{L_{yy}(\omega)L_{yy}(\omega_1)}(\chi^{(2)}_{\exp})_{ssp}\right)}{L'_{zz}(\omega)L'_{zz}(\omega_1)L'_{zz}(\omega_2)} \quad [1]$$

in our experimental geometry (angles of incidence and reflection all being 45°), where ssp (ppp) stands for s- (p-) polarized SFG output, s- (p-) visible input, and p- (p-) polarized IR input. ω, ω_1, and ω_2 denote the frequencies of the SFG ($\omega = \omega_1 + \omega_2$), visible, and IR fields, respectively. L_{xx} and L_{yy} are the xx and yy components of the Fresnel factors, respectively, while L'_{zz} is the ε'-uncorrected zz component of the Fresnel factor (19, 25) (SI Appendix, sections 1 and 9). The $\chi'^{(2)}_{zzz}$ spectrum can be further obtained from the simulated $(\chi^{(2)}_{\sim})_{zzz}$ spectrum via

$$\chi'^{(2)}_{zzz} = \frac{1}{\varepsilon'(\omega)\varepsilon'(\omega_1)\varepsilon'(\omega_2)}(\chi^{(2)}_{\sim})_{zzz}. \quad [2]$$

We note that the SFG spectral line shape of the zzz component is more strongly affected by the interfacial dielectric environment than the commonly probed xxz spectral components (12, 26). As such, the $\chi'^{(2)}_{zzz}$ spectrum is a sensitive probe for the interfacial dielectric function of water.

Results

Fig. 1A displays the complex $(\chi^{(2)}_{\exp})_{ssp}$ spectra of the O–H stretch mode at the air/water interface. The imaginary and real parts of $\chi^{(2)}$, denoted as Im$\chi^{(2)}$ and Re$\chi^{(2)}$, represent the absorptive and dispersive spectra, respectively. The Im$(\chi^{(2)}_{\exp})_{ssp}$ spectrum shows a sharp 3,700 cm^{-1} positive peak, a positive shoulder at 3,600 cm^{-1}, and a 3,100 to 3,500 cm^{-1} negative band, similar to a previous report (15). Fig. 1B shows the $(\chi^{(2)}_{\exp})_{ppp}$ spectra at the air/water interface. The Im$(\chi^{(2)}_{\exp})_{ppp}$ data show a sharp positive peak at 3,700 cm^{-1}, a 3,600 cm^{-1} negative peak, and a broad positive band below 3,500 cm^{-1}. By using these spectra, we obtained the Im$\chi'^{(2)}_{zzz}$ spectrum via Eq. 1, which is shown in Fig. 1G.

Next, we obtain the Im$\chi'^{(2)}_{zzz}$ spectrum from the simulation via Eq. 2. To do so, we need the simulated $(\chi^{(2)}_{\sim})_{zzz}$ spectra at the air/water interface and deduced ε' of water (25). Fig. 1C shows the $(\chi^{(2)}_{\sim})_{zzz}$ spectra with the POLI2VS model of water (SI Appendix, section 2). Two common models have been used to infer ε' from the dielectric function ε of bulk water. The slab model (25) (Fig. 1D) and the Lorentz model (19) (Fig. 1E) both assume that ε' is homogeneous. In the slab model, a vibrational chromophore is assumed to be half solvated, providing $\varepsilon' = \varepsilon(\varepsilon + 5)/(4\varepsilon + 2)$. For the fully solvated Lorentz

model, $\varepsilon' = \varepsilon$ (27). The resulting Re$(\varepsilon'(\omega_2))$ spectra in the O–H stretch frequency region are presented in Fig. 1F [see SI Appendix, Table S1 for $\varepsilon'(\Omega)$ and $\varepsilon'(\omega_1)$]. The Re$(\varepsilon'(\omega_2))$ line shapes are similar between the slab and Lorentz models, while the amplitude is ~50% larger in the Lorentz model than in the slab model. Fig. 1G plots the obtained Im$\chi'^{(2)}_{zzz}$ spectrum by using $(\chi^{(2)}_{\sim})_{zzz}$ spectra and ε' spectra.

The comparison of the Im$\chi'^{(2)}_{zzz}$ spectra (Fig. 1G) indicates that neither the Lorentz model nor the slab model provides a satisfactory agreement between the simulation and the experiment across the entire spectral range. The Lorentz model underestimates the 3,700 cm^{-1} peak amplitude, while the slab model overestimates the amplitude of the negative 3,100 to 3,500 cm^{-1} band. A similar trend can be seen in the SFG spectra simulated with the MB-pol model of water (SI Appendix, Fig. S5) (23). Because both POLI2VS and MB-pol models could reproduce the vibrational spectral features and amplitudes of bulk water (20, 21) (SI Appendix, section 3), as well as the structure of the air/water interface accurately (13, 28), disagreement between the processed experimental data and simulation data with the POLI2VS and MB-pol models of water can be ascribed to the breakdown of the homogeneous ε'-continuum assumption in the interfacial region (SI Appendix, section 11).

Interestingly, the two models can capture the trend in different spectral regions: the slab model somewhat reproduces the 3,700 cm^{-1} positive free O–H peak, while the Lorentz model captures the negative 3,100 to 3,500 cm^{-1} H-bonded O–H stretch band. As such, the different models appear to account for the dielectric environments locally, but none of the models can describe the environment over the entire spectral range. Clearly, the free O–H and H-bonded O–H stretch chromophores, originating from water molecules at different depths, experience different dielectric environments.

To better account for the varying dielectric environment, we consider different interfacial dielectric functions for different water species (19, 25) and recomputed the Im$\chi'^{(2)}_{zzz}$ spectra based on the obtained interfacial dielectric functions. We classified the SFG-active water molecules based on the number of hydrogen bonding donors (D) and acceptors (A); DA water molecules donate one H-bond and accept one H-bond, and in the same notation we classify DAA, DDA, and DDAA water molecules (29) (SI Appendix, section 4). The snapshot of these water molecules at the air/water interface is shown in Fig. 2A, indicating that various species are present at the air/water interface. The contributions of these species l ($l =$ DA, DAA, DDA, and DDAA) to Im$(\chi^{(2),l}_{\sim})_{zzz}$ are displayed in Fig. 2B. The free O–H stretch mode region is dominated by DA- and DAA-type molecules, while all the types of molecules contribute to the 3,100 to 3,500 cm^{-1} SFG feature.

Subsequently, we computed the individual interfacial dielectric function for each water species l, ε'_l. Within the Lorentz model in heterogeneous medium,

$$\varepsilon'_l = \frac{3\varepsilon\rho_{e0} + \varepsilon(\varepsilon - 1)\rho^l_e}{3\varepsilon\rho_{e0} - 2(\varepsilon - 1)\rho^l_e}, \quad [3]$$

$$\rho^l_e = \frac{\int D^l(z)\rho_e(z)\,dz}{\int D^l(z)\,dz}, \quad [4]$$

in the dc current limit, where ρ_{e0} and ρ^l_e denote the averaged electron densities of bulk water and of interfacial water species l, respectively, and ε is the dielectric function of bulk water. $D^l(z)$ and $\rho_e(z)$ represent the depth distributions of the SFG active water species l and electron density of water, respectively.
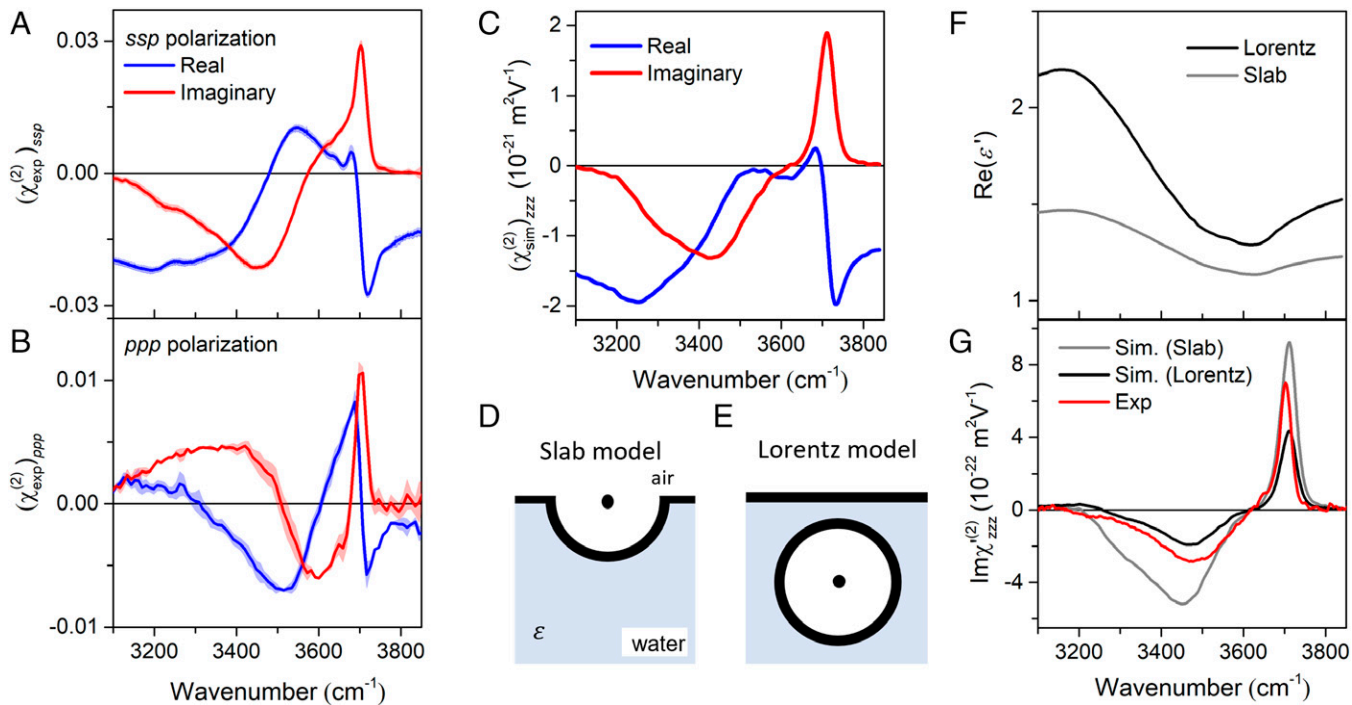
Fig. 1. SFG spectra at the air/water interface with homogeneous ε' models. (*A, B*) Measured $(\chi^{(2)}_{exp})_{ssp}$ (*A*) and $(\chi^{(2)}_{exp})_{ppp}$ (*B*) spectra of the air/water interface normalized by quartz signal. The shaded area represents the standard deviation of the measurement. (*C*) Simulated $(\chi^{(2)}_{sim})_{zzz}$ spectra with the POLI2VS model of water. (*D, E*) Schematic representation of the common models to estimate the interfacial dielectric function ε' using the slab model (*D*) and the Lorentz model (*E*). The point centered at the semi-circle/circle represents the position of the vibrational chromophore. (*F*) $\mathrm{Re}(\varepsilon'(\omega_2))$ spectra obtained from the slab and Lorentz models. (*G*) $\mathrm{Im}\chi'^{(2)}_{zzz}$ spectra at the air/water interface obtained from the experiments via Eq. **1** and from the simulations via Eq. **2**. Note the inadequacy of the two simple models to describe the experimental data.

We used this model for estimating the interfacial dielectric function at IR, visible, and SFG frequencies (25). The detailed calculation procedure is described in *SI Appendix*, sections 4–8. Note that a similar idea to model the interfacial dielectric constant was used in ref. 30, using the water density instead of the electron density of water. We consider the electron density because the dielectric function at these frequencies is dominated by the electronic rather than the nuclear wave functions.

To accurately obtain the $\rho_e(z)$, we took these directly from ab initio simulations and compared them to the $\rho_e(z)$ deduced from the water density profile based on the assumption of the Gaussian distribution of electrons around the nuclei. As can be seen from Fig. 2*C*, the $\rho_e(z)$ deduced from the water density, as obtained from the molecular dynamics (MD) simulations, agrees best with ab initio calculations when we assume a 0.5 Å SD of the Gaussian-shaped electron distribution. $\rho_e(z)$ is smeared out and more continuous than the water density (Fig. 2*C*).

Subsequently, Fig. 2*D* displays the depth distributions of the SFG active water species $D^l(z)$, i.e., water species contributing to a net nonzero dipole moment along the z axis in thermal average. The SFG active water molecules with a free O–H group such as the DA and DAA species are located close to the air region, while those with no free O–H group such as the DDA and DDAA species are located near the bulk water region. The difference in the maxima of the DAA and DDA species distributions is just ~1 Å, but this critically affects the interfacial dielectric constant they experience because $\rho_e(z)$ changes drastically in this depth region. Computing the averaged electron density, ρ_e^l, surrounding the different species based on their spatial distribution $D^l(z)$ (*SI Appendix*, sections 7 and 8) via Eq. **4**, we obtained $\mathrm{Re}(\varepsilon_l')$ according to Eq. **3**. The computed $\mathrm{Re}(\varepsilon_l')$ spectra in the O–H stretch region are shown

in Fig. 2*E*. This comparison demonstrates that the difference in the $\mathrm{Re}(\varepsilon_l')$ spectra for the DAA and DDA species is larger than that for the DDA and DDAA species, despite the smaller separation of the depth position of the DAA and DDA species than that of the DDA and DDAA species.

The $\mathrm{Re}(\varepsilon_l')$ spectra also indicate that the dielectric environment of DDAA and DDA molecules can be well approximated by the Lorentz model (bulk), while the dielectric environment that the DA and DAA molecules experience is closer to that predicted by the slab model. This notion is consistent with our finding that the slab model reproduces the 3,700 cm^{-1} free O–H stretch peak, and the Lorenz model reproduces the 3,400 cm^{-1} H-bonded O–H stretch peak (Fig. 1*G*).

Combining the $(\chi^{(2),l}_{sim})_{zzz}$ and ε_l' spectra, we can compute $\chi'^{(2)}_{zzz}$ via

$$\chi'^{(2)}_{zzz} = \sum_l \frac{1}{\varepsilon_l'(\omega)\varepsilon_l'(\omega_1)\varepsilon_l'(\omega_2)}(\chi^{(2),l}_{sim})_{zzz} \qquad \textbf{[5]}$$

instead of Eq. **2**. The simulated vs. experimentally obtained $\chi'^{(2)}_{zzz}$ spectra are shown in Fig. 2*F*. The quantitative agreement for both the line shapes and amplitudes of the $\mathrm{Im}\chi'^{(2)}_{zzz}$ spectra manifests that Eq. **3** describes the interfacial dielectric well; the variation of the interfacial electron density provides an excellent a priori prediction of the interfacial dielectric function ε_l', allowing us to reproduce the SFG spectra. Here we assume that the inconsistency between experimental and simulated spectra (Fig. 1*G*) arises from the homogeneous interfacial dielectric functions.

Discussion

In the *Results*, we established that the interfacial dielectric function at infrared and optical frequencies varies in the interfacial
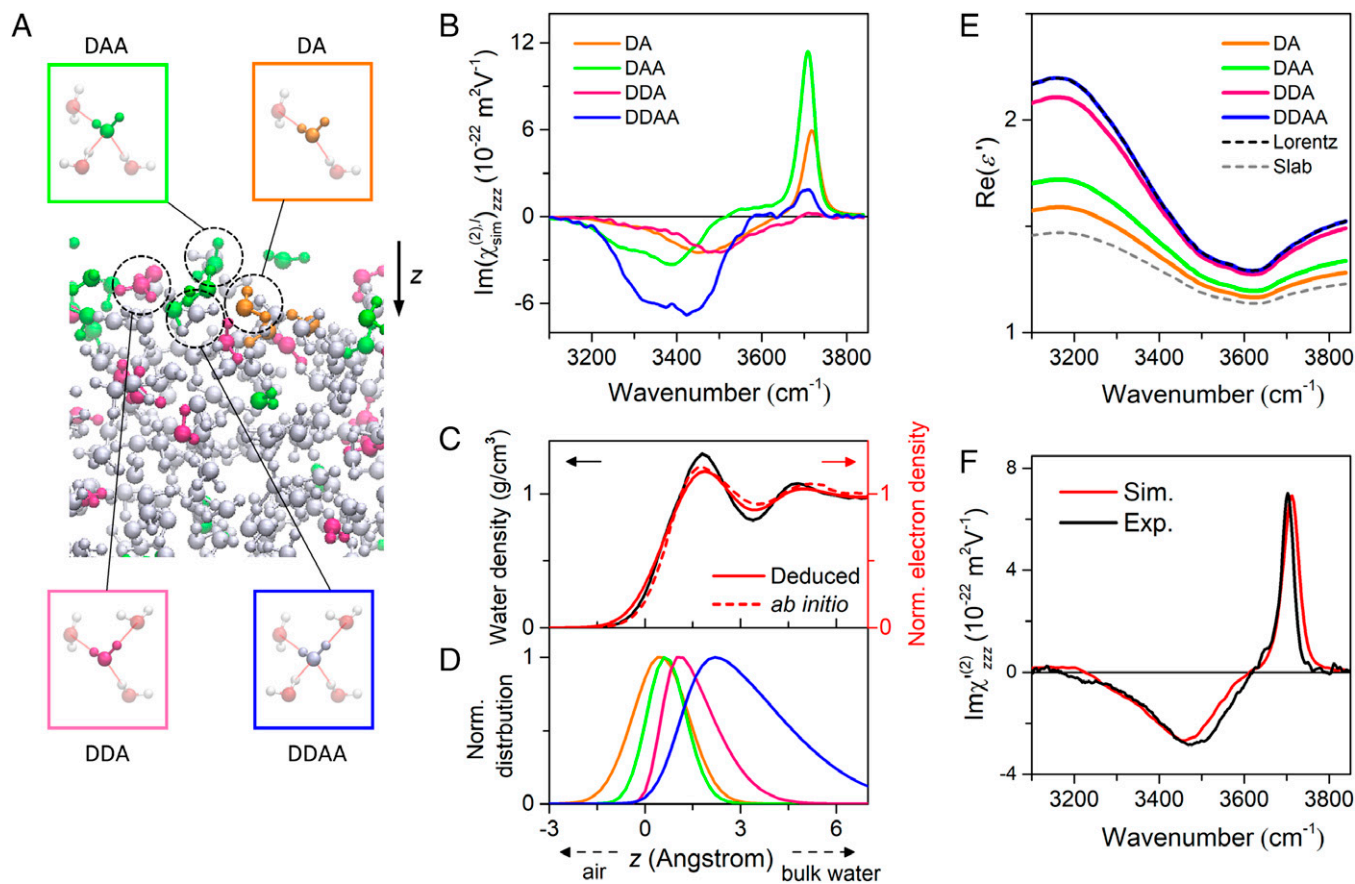
Fig. 2. SFG spectra at the air/water interface with varying ε' model. (A) Snapshot of the air/water interface obtained from the simulation. Insets show the typical H-bond conformations of the DA, DAA, DOA, and DDAA water species. (B) $\mathrm{Im}(\chi^{(2),l}_{sim})_{zzz}$ spectra contributions for various water species. (C) Depth profiles of simulated water density (black), deduced electron density of water with a Gaussian distribution $\rho_e(z)$, and electron density computed at the *ab initio* level of theory at the air/water interface. (D) Depth profiles of the SFG active water species I, $D^I(z)$. The origin point ($z = 0$) was defined as the position of the instantaneous surface (49). (E) $\mathrm{Re}(\varepsilon'_l)$ spectra for water species I together with the dielectric spectra calculated from Lorentz and slab models. (F) Comparison of the simulated and experimentally obtained $\mathrm{Im}\chi'^{(2)}_{zzz}$ spectra.

region on angstrom-length scales, and its variation can be approximated well by the electron density profile. Now we proceed with exploring potential macroscopic consequences of the interfacial dielectric function. In fact, such drastic variation of the interfacial dielectric medium has been shown to markedly affect the electric double-layer formed near charged interfaces (4, 31). Given that also in the dc limit, the dielectric permittivity correlates with the local water density (4, 11), we test the consequences of an angstrom-length scale variation of the permittivity according to Eq. **3** on the electrostatic double-layer potential.

Here we consider two model interfaces of the pristine graphene and holey graphene/electrolyte solution interfaces (Fig. 3 *A* and *B*). We study these two interfaces to investigate how interfacial corrugation affects the dielectric profile because the capacitances of the pristine and holey graphene differ significantly (32). The depth profiles of the water density obtained from the ab initio MD (AIMD) simulation and the deduced electron density at these interfaces are displayed in Fig. 3 *C* and *D*, respectively. The water density profile near the pristine graphene surface is consistent with previous MD results (33–36). The water density profile shows a sharp peak near the graphene sheets ($z = 3$ Å), while the electron density is smeared out due to the distribution of the electron cloud. For holey graphene, the penetration of water to the nanopore blurs the water density profile due to the water molecules inside the hole (highlighted by circles in Fig. 3*B*), inducing a more gradual rise in the electron density profile near the interface. Subsequently,

we computed the depth variation of the dielectric function with Eq. **3** using the depth profile of water's electron density (*SI Appendix*, section 10). The data are displayed in Fig. 3*C*. For both systems, the dielectric function oscillates near the graphene layer, unlike what is assumed for double-layer models based on the homogeneous dielectric function (4). Note that while the effect of penetration of water in the holes of graphene on the electron density profile is limited, it gives rise to a substantial variation in the dielectric function at the surface.

Using these three dielectric profiles under the assumption that the overall peak profile of the water density at these interfaces is insensitive to the small applied voltage (~100 mV) based on ref. 34, we calculated the electrostatic potential by solving the Poisson–Boltzmann equation for a fixed, moderate surface charge density (-4.8 mC m^{-2}) in the presence of 0.1 M monovalent electrolytes (4, 37). The variation of the electrostatic potential is shown in Fig. 3*D*. The figure indicates that the potential changes moderately over the entire interfacial region in the homogeneous dielectric medium model, while the potential varies drastically near $z = 0$ in the oscillatory dielectric medium models. In fact, the surface potential ($z = 0$) reaches -100 mV in the oscillatory dielectric medium for the pristine graphene, ~10 times larger than the homogeneous dielectric medium model. For pristine graphene, the electrostatic potential decays through the two layers. First, the drastic potential drop occurs within a few angstroms thickness generated by the excluded volume of molecules in between the graphene and
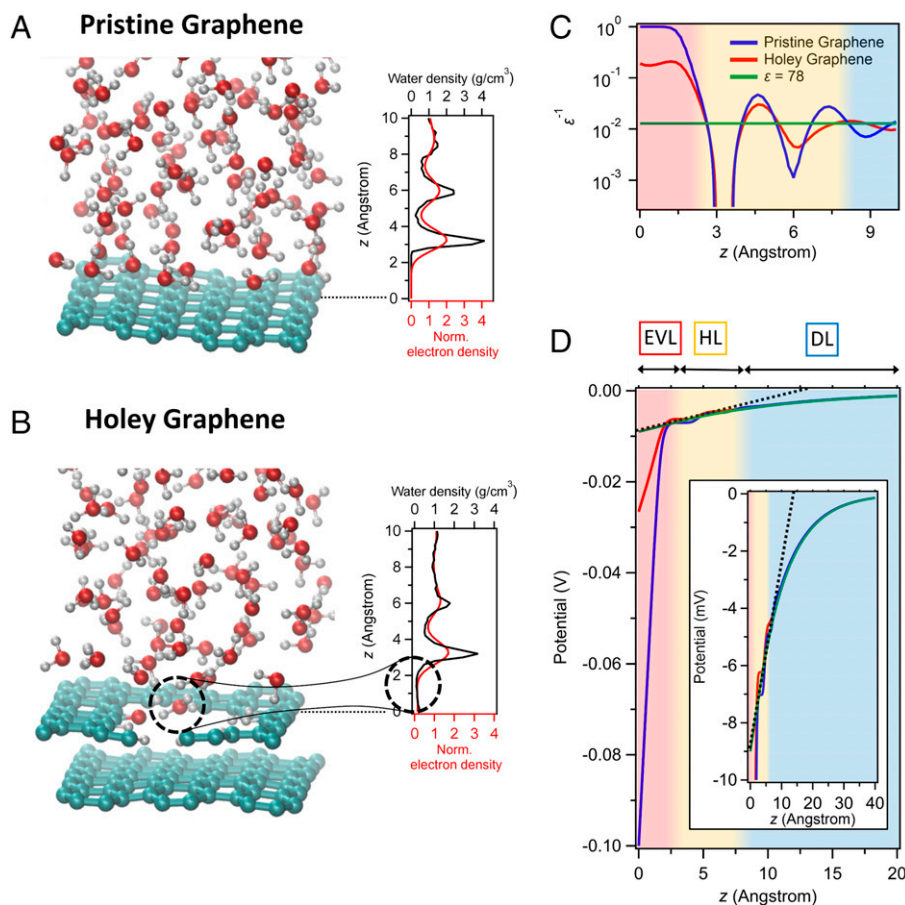
Fig. 3. Model calculation of surface potential profile at the charged graphene/water interfaces. (*A, B*) Snapshots of the pristine graphene/water (*A*) and the holey graphene/water (*B*) interfaces together with their density profiles of water and normalized electron density profiles. (*C*) Depth-dependent inverse dielectric functions deduced from the electron density profiles shown in **a** and **b** and homogeneous inverse dielectric function ($\varepsilon = 78$). The origin point ($z = 0$) was set to the position of the carbon atoms composing the first layer of pristine and holey graphene sheets. Interfacial dielectric profile calculated via eq. **3** for the pristine (blue) and holey graphene (red) samples as well as the homogeneous dielectric profile (black). (*D*) Comparison of the surface potential profile under a constant surface charge with an oscillatory dielectric medium model for the pristine graphene (blue), oscillatory dielectric medium model for the holey graphene (red), and homogeneous dielectric medium model (black). The black dotted line is obtained from the fit of the green curves in 0 Å < z < 3 Å. The departure of the deviation between the dotted line and green curve is the interface of HL and DL, while the departure of the deviation of green, red, blue curves is the interface of the EVL and DL.

topmost water layer (excluded volume layer [EVL]) (11). The potential drops linearly in the second layer, ranging from ∼3 to ∼8 Å from the interface, due to the ion accumulation in the Helmholtz layer (HL) (8). For $z > 8$ Å, the surface potential decays in a nonlinear fashion, which is typical for the diffuse layer (DL). Fig. 3*D* illustrates that the main difference in the surface potential arises from the EVL. The dielectric constant in the interfacial region, which is nearly unity, increases the capacitance, generating a drastic increase in the surface potential. As such, the charged flat interfaces create an electric triple layer, and EVL has a dominant role in determining the capacitance.

The holey graphene has some water molecules inside the hole of the graphene and between the hole and the topmost layer of water (Fig. 3*B*). These water molecules make the dielectric constant more than unity in the EVL. Because the dielectric constant of water is high, a small density of water (0.1 to 0.2 g/cm³ in our model calculation) is sufficient to reduce the required voltage and thus increase the capacitance. As such, the capacitance of the holey graphene modeled here is higher by a factor of 4 to 5 than the capacitance of the pristine graphene. This observation agrees with the experimental data (32). As such, the mechanism underlying the high capacitance of holey graphene is that the water inside the holes of the graphene

generates the >1 dielectric constant in the EVL. Such an electric triple-layer model would be further helpful in accounting for the anomalous behavior of the capacitance with a subnanometer pore size of the carbon capacitance (38).

The electric triple-layer model presented here differs from Grahame's triple-layer model widely accepted in electrochemistry, which consists of inner Helmholtz, outer Helmholtz, and diffuse layers (8). In Grahame's model, the inner Helmholtz layer consists of moieties adsorbed on the surface, altering the double-layer capacitance. In contrast, the current model indicates that the vacuum space of EVL determines the double-layer capacitance without assuming specifically adsorbed moieties and is instead determined by the physical properties of the surface, e.g., the flatness of the surface and the defect density on the surface. Finally, we would like to stress the importance of the surface flatness for the modulation of the capacitance; for structurally rough interfaces such as liquid/liquid interfaces (39, 40), the electron density profiles are commonly rather smooth, and as such, the modeled dielectric profile will vary less with distance as compared to the flat interface of the graphene/water, leading to dramatic enhancement of the capacitance.

In summary, by comparing the experimental and simulated amplitude and line shapes of the SFG spectra at the air/water interface, we find a steep gradient of the interfacial dielectric

function is across the SFG-active ~1-Å water layer. Such drastic change of the interfacial dielectric medium generates a triple-layer structure of surface potential: EVL, Helmholtz layer, and diffuse layer. The EVL critically controls the surface potential. We show that this EVL explains why holey graphene shows a higher capacitance than pristine graphene. This highlights the potential to engineer defects into electrodes for improving the double-layer capacitance and is essential for catalytic reactions on graphene-derived materials and proton transport through graphene.

Materials and Methods

Heterodyne-Detected SFG Measurement. The $\chi^{(2)}$ spectra were measured using a heterodyne-detected SFG setup. We used a part of the output from a 1-kHz femtosecond Ti:Sapphire laser system (Spectra-Physics) to pump a commercial optical parametric amplifier (TOPAS SHBS-400, Spectra-Physics) to generate a broadband mid-IR pulse and guided the other part of the output to a pulse shaper to generate a narrowband visible pulse. First, the IR pulse with its frequency of ω_2 (bandwidth ~350 cm^{-1}) and visible pulse with its frequency of ω_1 (bandwidth ~12 cm^{-1} at center wavelength 800 nm) were focused onto a 20-μm-thick y-cut quartz plate to generate the local oscillator (LO). The ω_1, ω_2, and LO beams were focused again onto the sample surface with all the incident angles of 45° after copropagating through a phase modulator which delayed the LO pulse relative to ω_1 and ω_2 pulses by 2 ps. The spectral interferogram created by SF beam from the sample and LO beam was detected by a charge-coupled device. We obtained the complex $\chi^{(2)}$ spectra by normalizing the sample signal by the signal of the z-cut quartz crystal. Water was obtained from a Milli-Q water purification system (18.2 MΩ cm resistivity).

MD Simulation at Air/Water Interface with POLI2VS Model of Water. We used the POLI2VS force field model of water to simulate the SFG spectra at the air/water interface (20). The size of the simulation cell was 32.0 Å × 32.0 Å × 110 Å. This cell contained 2,048 water molecules, generating the water slab with its thickness of ~60 Å. We generated the independent 20 initial coordinates and ran the 1-ns MD simulations for individual initial coordinates for equilibrating the systems. After that, we ran the >2.6-ns MD simulations for each configuration, generating a total of >52-ns trajectories. These 52-ns MD trajectories were used for analyzing the simulation data. The time step for integrating equations of motion was set to 0.4 fs. We recorded the trajectories of water molecules, molecular dipole moment, and polarizability every 4 fs (every 10 MD steps). The molecular dipole moment and polarizability can be computed within the POLI2VS force field model. The simulations were performed in the canonical ensemble. The temperature was set to 300 K and was controlled with the Nosé–Hoover thermostat (41) with 10 chains.

AIMD Simulation at Pristine Graphene/Water and Holey Graphene/Water Interfaces. We carried out AIMD simulations for the systems of pristine graphene/D$_2$O (W-pG) interface and holey graphene/D$_2$O (W-hG) interface. The cell sizes of both W-pG and W-hG systems were set to 12.765 Å × 14.736 Å × 40.0 Å. The W-pG system consists of a single layer of graphene (72 carbon

atoms) and 121 water molecules, while the W-hG system consists of one layer of graphene (72 carbon atoms), one layer of holey graphene (53 carbon atoms, 10 hydrogen atoms, and 1 oxygen atom), and 121 water molecules. For the structure of holey graphene, we used one of the oxygen-terminated structures based on the graphene oxide structure (42) as holey graphene with high capacity is prepared from graphene oxide (32). In the W-hG systems, the pristine graphene and holey graphene were stacked via the AB stacking conformation. We generated two independent conformations for the W-pG systems and six independent conformations for the W-hG systems. We did not put additional charges on the pristine/holey graphene in the AIMD simulation.

For the AIMD simulation, we used the BLYP exchange correlation functional together with the Grimme's D3(0) van der Waals correction (43). We employed the QUICKSTEP method (44) implemented in the CP2K code (45). For the Gaussian part of the basis set, we used the MOLOPT shorter range double zeta for valence electrons plus polarization function (DZVP) basis set (46) for the carbon atoms, while we used the triple zeta for valence electrons plus double polarization function (TZV2P) basis set for other atoms. We set the plane wave density cutoff to 320 Ry. The norm-conserving Goedecker–Teter–Hutter pseudopotentials (47) were used for describing the core electrons. We performed the AIMD simulation in the canonical ensemble, where the target temperature was set to 300 K with canonical sampling through a velocity rescaling thermostat (48, 49). The time step for integrating the equations of motions was set to 0.5 fs. We equilibrated the sample for >20 ps, and then we obtained the ~30-ps AIMD trajectory for each sample.

Finally, we would like to note that we include one oxygen atom for the holey graphene to allow water molecule(s) to fill the space generated by the hole of the graphene. If all the carbon atoms surrounding the hole are terminated by hydrogen atoms, water molecules do not enter the hole of the graphene, due to the high surface tension of water.

Author affiliations: ^{a}Molecular Spectroscopy Department, Max Planck Institute for Polymer Research, 55128 Mainz, Germany; and ^{b}Division of Frontier Materials Science, Graduate School of Engineering Science, Osaka University, Toyonaka 60-8531, Japan

1. S. Narayan *et al.*, "On water": Unique reactivity of organic compounds in aqueous suspension. *Angew. Chem. Int. Ed. Engl.* **44**, 3275–3279 (2005).
2. J. Zhong, M. Kumar, J. S. Francisco, X. C. Zeng, Insight into chemistry on cloud/aerosol water surfaces. *Acc. Chem. Res.* **51**, 1229–1237 (2018).
3. T. Mouterde *et al.*, Molecular streaming and its voltage control in Ångström-scale channels. *Nature* **567**, 87–90 (2019).
4. D. J. Bonthuis, S. Gekle, R. R. Netz, Dielectric profile of interfacial water and its effect on double-layer capacitance. *Phys. Rev. Lett.* **107**, 166102 (2011).
5. S. Hu *et al.*, Proton transport through one-atom-thick crystals. *Nature* **516**, 227–230 (2014).
6. J. L. Achtyl *et al.*, Aqueous proton transfer across single-layer graphene. *Nat. Commun.* **6**, 6539 (2015).
7. J. Xu *et al.*, Transparent proton transport through a two-dimensional nanomesh material. *Nat. Commun.* **10**, 3971 (2019).
8. G. Gonella *et al.*, Water at charged interfaces. *Nat. Rev. Chem.* **5**, 466–485 (2021).
9. L. Fumagalli *et al.*, Anomalously low dielectric constant of confined water. *Science* **360**, 1339–1342 (2018).
10. V. G. Artemov *et al.*, Anomalously high proton conduction of interfacial water. *J. Phys. Chem. Lett.* **11**, 3623–3628 (2020).
11. J.-F. Olivieri, J. T. Hynes, D. Laage, Confined water's dielectric constant reduction is due to the surrounding low dielectric media and not to interfacial molecular ordering. *J. Phys. Chem. Lett.* **12**, 4319–4326 (2021).
12. Q. Du, R. Superfine, E. Freysz, Y. R. Shen, Vibrational spectroscopy of water at the vapor/water interface. *Phys. Rev. Lett.* **70**, 2313–2316 (1993).
13. F. Tang *et al.*, Molecular structure and modeling of water-air and ice-air interfaces monitored by sum-frequency generation. *Chem. Rev.* **120**, 3633–3667 (2020).
14. S. Pezzotti *et al.*, Molecular fingerprints of hydrophobicity at aqueous interfaces from theory and vibrational spectroscopies. *J. Phys. Chem. Lett.* **12**, 3827–3836 (2021).
15. S. Nihonyanagi *et al.*, Accurate determination of complex $\chi(2)$ spectrum of the air/water interface. *J. Chem. Phys.* **143**, 124707 (2015).
16. P. A. Pieniazek, C. J. Tainter, J. L. Skinner, Interpretation of the water surface vibrational sum-frequency spectrum. *J. Chem. Phys.* **135**, 044701 (2011).
17. T. Ishiyama, A. Morita, Analysis of anisotropic local field in sum frequency generation spectroscopy with the charge response kernel water model. *J. Chem. Phys.* **131**, 244714 (2009).
18. S. Pezzotti, D. R. Galimberti, M.-P. Gaigeot, 2D H-bond network as the topmost skin to the air-water interface. *J. Phys. Chem. Lett.* **8**, 3133–3141 (2017).
19. A. Morita, *Theory of Sum Frequency Generation Spectroscopy* (Springer, Singapore, 2018).
20. T. Hasegawa, Y. Tanimura, A polarizable water model for intramolecular and intermolecular vibrational spectroscopies. *J. Phys. Chem. B* **115**, 5545–5553 (2011).
21. G. R. Medders, F. Paesani, Infrared and Raman spectroscopy of liquid water through "first-principles" many-body molecular dynamics. *J. Chem. Theory Comput.* **11**, 1145–1154 (2015).
22. Y. Nagata *et al.*, The surface roughness, but not the water molecular orientation varies with temperature at the water-air interface. *Phys. Chem. Chem. Phys.* **17**, 23559–23564 (2015).
23. D. R. Moberg, S. C. Straight, F. Paesani, Temperature dependence of the air/water interface revealed by polarization sensitive sum-frequency generation spectroscopy. *J. Phys. Chem. B* **122**, 4356–4365 (2018).

24. K. Niu, R. A. Marcus, Sum frequency generation, calculation of absolute intensities, comparison with experiments, and two-field relaxation-based derivation. *Proc. Natl. Acad. Sci. U.S.A.* **117**, 2805–2814 (2020).

25. X. Zhuang, P. B. Miranda, D. Kim, Y. R. Shen, Mapping molecular orientation and conformation at interfaces by surface nonlinear optics. *Phys. Rev. B Condens. Matter Mater. Phys.* **59**, 12632–12640 (1999).

26. W. Gan, D. Wu, Z. Zhang, R. R. Feng, H. F. Wang, Polarization and experimental configuration analyses of sum frequency generation vibrational spectra, structure, and orientational motion of the air/water interface. *J. Chem. Phys.* **124**, 114705 (2006).

27. G. M. Hale, M. R. Querry, Optical constants of water in the 200-nm to 200-microm wavelength region. *Appl. Opt.* **12**, 555–563 (1973).

28. S. Sun et al., Orientational distribution of free O-H groups of interfacial water is exponential. *Phys. Rev. Lett.* **121**, 246101 (2018).

29. F. Tang et al., Definition of free O-H groups of water at the air-water interface. *J. Chem. Theory Comput.* **14**, 357–364 (2018).

30. K. Shiratori, A. Morita, Molecular theory on dielectric constant at interfaces: A molecular dynamics study of the water/vapor interface. *J. Chem. Phys.* **134**, 234705 (2011).

31. H. Zhu, A. Ghoufi, A. Szymczyk, B. Balannec, D. Morineau, Anomalous dielectric behavior of nanoconfined electrolytic solutions. *Phys. Rev. Lett.* **109**, 107801 (2012).

32. T. Liu, L. Zhang, B. Cheng, X. Hu, J. Yu, Holey graphene for electrochemical energy storage. *Cell Reports Phys. Sci.* **1**, 100215 (2020).

33. T. Ohto, H. Tada, Y. Nagata, Structure and dynamics of water at water-graphene and water-hexagonal boron-nitride sheet interfaces revealed by ab initio sum-frequency generation spectroscopy. *Phys. Chem. Chem. Phys.* **20**, 12979–12985 (2018).

34. Y. Zhang, H. B. de Aguiar, J. T. Hynes, D. Laage, Water structure, dynamics, and sum-frequency generation spectra at electrified graphene interfaces. *J. Phys. Chem. Lett.* **11**, 624–631 (2020).

35. G. Tocci, L. Joly, A. Michaelides, Friction of water on graphene and hexagonal boron nitride from ab initio methods: Very different slippage despite very similar interface structures. *Nano Lett.* **14**, 6872–6877 (2014).

36. L. Joly, R. H. Meißner, M. Iannuzzi, G. Tocci, Osmotic transport at the aqueous graphene and hBN interfaces: Scaling laws from a unified, first-principles description. *ACS Nano* **15**, 15249–15258 (2021).

37. M. A. Brown et al., Determination of surface potential and electrical double-layer structure at the aqueous electrolyte-nanoparticle interface. *Phys. Rev. X* **6**, 011007 (2016).

38. Y. Xu et al., Holey graphene frameworks for highly efficient capacitive energy storage. *Nat. Commun.* **5**, 4554 (2014).

39. L. Lin et al., Ion pairing and molecular orientation at liquid/liquid interfaces: Self-assembly and function. *J. Phys. Chem. B* **126**, 2316–2323 (2022).

40. Z. Liu et al., Squeezing out interfacial solvation: The role of hydrogen-bonding in the structural and orientational freedom of molecular self-assembly. *J. Phys. Chem. Lett.* **13**, 2273–2280 (2022).

41. G. J. Martyna, M. L. Klein, M. Tuckerman, Nosé–Hoover chains: The canonical ensemble via continuous dynamics. *J. Chem. Phys.* **97**, 2635–2643 (1992).

42. C. Su, K. P. Loh, Carbocatalysts: Graphene oxide and its derivatives. *Acc. Chem. Res.* **46**, 2275–2285 (2013).

43. S. Grimme, S. Antony, S. Ehrlich, H. Krieg, A consistent and accurate ab initio parametrization of density functional dispersion correction (DFT-D) for the 94 elements H-Pu. *J. Chem. Phys.* **132**, 154104 (2010).

44. J. Vandevondele et al., Quickstep: Fast and accurate density functional calculations using a mixed Gaussian and plane waves approach. *Comput. Phys. Commun.* **167**, 103–128 (2005).

45. J. Hutter, M. Iannuzzi, F. Schiffmann, J. VandeVondele, CP2K: Atomistic simulations of condensed matter systems. *Wiley Interdiscip. Rev. Comput. Mol. Sci.* **4**, 15–25 (2014).

46. J. VandeVondele, J. Hutter, Gaussian basis sets for accurate calculations on molecular systems in gas and condensed phases. *J. Chem. Phys.* **127**, 114105 (2007).

47. S. Goedecker, M. Teter, J. Hutter, Separable dual-space Gaussian pseudopotentials. *Phys. Rev. B Condens. Matter* **54**, 1703–1710 (1996).

48. G. Bussi, D. Donadio, M. Parrinello, Canonical sampling through velocity rescaling. *J. Chem. Phys.* **126**, 014101 (2007).

49. A. P. Willard, D. Chandler, Instantaneous liquid interfaces. *J. Phys. Chem. B* **114**, 1954–1958 (2010).